Nanoscale Advances

ROYAL SOCIETY OF CHEMISTRY

PAPER

View Article Online
View Journal | View Issue

Cite this: *Nanoscale Adv.*, 2025, **7**, 3293

The role of coating layers in gold nanorods' radioenhancement: a Monte Carlo analysis

Taheri A., *[a] Khandaker M. U., *[abc] Rabus H., [d] Moradi F.[e] and Bradley D. A.[af]

Gold nanoparticles are promising radiosensitizing agents for nanoparticle-enhanced radiotherapy (NPRT). The coating layer on these nanoparticles can significantly influence their physicochemical characteristics and biological behavior. This study investigates the influence of various coating layers on the radioenhancement efficiency of gold nanorods by modeling the physical interactions and chemical reactions involved. We conducted Monte Carlo simulations using the TOPAS code to model secondary electron generation in gold nanorods exposed to 100 kVp X-rays. Through a multiscale approach, the dose contribution, electron spectrum, and *G*-values of radiolytic species were determined. Four conventional coating materials were examined and compared to a non-coated nanorod. The simulation results indicate that the addition of coating layers decreases the additional dose due to the gold nanorods by up to 7% across all materials. The assessment of electron spectra revealed that 1% to 8% of electrons with energies below 3.5 keV were absorbed within the various coating layers. In contrast, higher-energy electrons were mainly unaffected. The total *G*-values for all radiolytic species remained generally unchanged with the addition of the coating layer, regardless of the material used. However, increasing the coating thickness slightly increased the relative yield of chemical species at times beyond 10 ns post-irradiation. While the addition of a coating layer generally resulted in a decrease in electron fluence and dose contribution, the reduction was not as substantial as expected from results previously reported in the literature. This suggests that, from the physics perspective, the influence of coating layers on radioenhancement may be less pronounced than previously believed. Additionally, the observed increase in total *G*-values with thicker coatings emphasizes the need for further investigation into the effects of coatings on radiolytic species.

Received 5th March 2025
Accepted 3rd April 2025

DOI: 10.1039/d5na00220f

rsc.li/nanoscale-advances

Introduction

Radiotherapy (RT) is a major cancer treatment modality, prescribed for over half of all cancer cases.[1] However, its effectiveness can be limited by many factors, such as dose constraints, the inherent radioresistance of certain tumors, and radiation toxicity.[2–4] Among recent strategies to enhance patient outcomes, nanoparticle-enhanced radiotherapy (NPRT) has emerged as a promising approach for amplifying radiation effects and improving tumor suppression.[5–7] This enhancement mainly occurs through local radiation dose amplification and increased production of reactive oxygen species (ROS), leading to enhanced DNA damage and cell death.

Potential enhancement effects of metallic nanoparticles (MNPs) were originally attributed to physical dose enhancement predicted at keV photon energies.[8] Various approaches have been proposed for quantifying the effects of MNPs which are often referred to as radiosensitization.[9] However, the concept of radiosensitization relates to the use of specific agents that amplify the relative biological effectiveness of ionizing radiation through multiple mechanisms, ultimately enhancing radiation-induced cellular damage.[10] These mechanisms can be categorized into physical effects (photoelectric interactions and Auger electron cascades), chemical processes (enhanced ROS production and catalytic surface reactions), and biological responses (cellular uptake modulation and DNA repair inhibition). While the term "radiosensitization" is commonly applied across the literature, including in studies unrelated to biological effects, we adopt the more specific term "radioenhancement" for this study, as our investigation focuses exclusively on physical and chemical mechanisms.[11]

Various high atomic number metal nanoparticles (MNPs) have been investigated for NPRT.[12–16] Among them, gold

[a]*Applied Physics and Radiation Technologies Group, CCDCU, Faculty of Engineering and Technology, Sunway University, 47500 Bandar Sunway, Selangor, Malaysia. E-mail: alitmedical@gmail.com; mayeenk@sunway.edu.my*

[b]*Faculty of Graduate Studies, Daffodil International University, Daffodil Smart City, Birulia, Savar, Dhaka 1216, Bangladesh*

[c]*Department of Physics, College of Science, Korea University, 145 Anam-ro, Seongbuk-gu, Seoul, 02841, Republic of Korea*

[d]*Physikalisch-Technische Bundesanstalt (PTB), 10587 Berlin, Germany*

[e]*Radiation Dosimetry Research Group, Faculty of Engineering, Multimedia University, Jalan Multimedia, 63100, Cyberjaya, Malaysia*

[f]*School of Mathematics and Physics, University of Surrey, Guildford, GU27XH, UK*

nanoparticles (AuNPs) have garnered particular interest since their introduction as potential radiosensitizers by Hainfeld *et al.*[17] AuNPs offer several advantages, including versatile synthesis methods, various forms and sizes, diverse surface functionalization options, chemical stability, low toxicity, and high biocompatibility.1[18–21] The radioenhancement potential of AuNPs depends significantly on their characteristics, including size, shape, concentration, localization, and surface functionalization.[22] Gold nanorods were chosen for this study due to their versatility in cancer treatment, particularly their potential for synergistic photothermal and radiation therapy. In addition, their radiosensitization efficiency was shown to be comparable to that of gold nanospheres of the same mass.[15] This work builds upon previous studies[15,22,23] investigating the radioenhancement properties of metallic nanorods by further exploring the influence of surface coatings on their efficacy.

The coating layer can influence radioenhancement efficiency through various mechanisms, including physical, chemical, and biological effects. Physically, it can shield low-energy secondary electrons and alter surface Plasmon resonance. Chemically, it may impact ROS generation and scavenging and catalyze the redox reactions. Biologically, the selective delivery, cellular uptake, and biodistribution, as well as cell signaling pathways and immune responses can be affected by the coating material.[24–27] These interactions highlight the importance of surface functionalization, which plays a crucial role in stability, biocompatibility, cytotoxicity, and optimized cell internalization.[28,29] In the context of ROS reactions, some coating materials may exhibit antioxidant properties that scavenge ROS, while others can enhance ROS production through redox groups.[30,31]

It is also important to note that in biological environments, nanoparticle coatings can undergo significant alterations. When introduced to cells, nanoparticles become naturally coated with a layer of biomolecules, primarily proteins, forming what is known as a 'biomolecular corona' or 'protein corona'. This corona can significantly influence nanoparticle–cell interactions, cellular uptake, biodistribution, and ultimately therapeutic efficacy.[32] Additionally, the original coating layer may be degraded by serum proteins,[33] and also due to highly localized interactions with ionizing radiation.[34]

Despite the inherent bias arising from the typically higher cellular uptake of coated nanoparticles, *in vitro* and *in vivo* experimental studies have provided valuable insights into the impact of coating on radiosensitization (Table 1). Key findings indicate that while coated AuNPs often show improved cellular uptake and cytotoxicity,[33,35] the coating layer can reduce radioenhancement efficiency by absorbing low-energy secondary electrons generated inside the nanoparticle upon irradiation.[36,37] Studies have also shown that coating thickness, density, and material composition significantly affect DNA damage by reducing the number of secondary electrons and ROS generation.[30,33]

Computer simulations complement experimental studies by overcoming practical limitations and offering detailed insights into the complex physical and chemical interactions of the radioenhancement process. Monte Carlo (MC) simulations, particularly using track structure (TS) codes,[44] have been instrumental in this context.[45–48] Studies using various MC codes (summarized in Table 1) have demonstrated that coating layers can effectively absorb a notable portion of secondary electrons[41] and reduce dose enhancement,[39] with effects being more pronounced for smaller AuNPs and lower incident photon energies.

Among the several TS simulation tools, Geant4-DNA toolkit[49–54] stands out as a widely used, validated TS code. However, studies using this code have yielded contrasting results. He and Chow[38] found no significant impact of coating materials on dose enhancement, which was associated with the typically low atomic number of these materials. In contrast, Peukert *et al.*[42] observed decreased radioenhancement with increasing PEG and silica coating thickness, both in terms of dose and radiolysis products. These contradictory findings may be attributed to different methodological approaches, with results potentially affected by limitations such as distance-dependent measurements and simulation geometries that fail to assure charged particle equilibrium (CPE) in the absence of NPs. Lack of CPE can greatly bias the dose enhancement ratios and result in unrealistically high values[55] that require corrections to estimate the proper dose enhancement under CPE.[34,56,57] Additionally, owing to the multiscale nature of their simulations, the interactions of the incoming beam with the coating layer were not taken into account. Consequently, it appears that the impact of the coating material on dose enhancement was overestimated in Peukert *et al.*,[42] and corrections would be needed for a more accurate assessment.

Despite the potential of coating layers to influence radioenhancement efficiency, a limited number of studies have focused specifically on the coating materials. Almost all the reviewed studies agree that the coating layer leads to the absorption of secondary electrons, resulting in the reduction of dose and radiolytic yield enhancement (Table 1). However, many other aspects have not been thoroughly investigated, such as detailed electron spectra, the effect of different coating materials on electron absorption, and the assessment of chemical reactions. To address these gaps, the present study examines the influence of the coating layer on the radioenhancement properties of gold nanorods (AuNRs). Four frequently used coating materials, namely silica (SiO_2), polyethylene glycol (PEG, $C_{2n}H_{4n+2}O_{n+1}$), polyethyleneimine (PEI, $(C_2H_5N)_n$), and cetyltrimethylammonium bromide (CTAB, $C_{19}H_{42}BrN$), at thicknesses of 25 and 50 nm were examined. This study used the TOPAS code[58] and its TOPAS-nBio extension[59,60] for the simulations. It is a follow-up to our previous works comparing the radioenhancement properties of gold nanorods with nanospheres and other MNPs.[15,23] The TOPAS code was selected for this study as it provides a user-friendly interface while fully incorporating the physics models and databases of Geant4, including Geant4-DNA and modeling chemical and biological reactions, making it particularly beneficial for nanoparticle radioenhancement studies.[61–65] The deposited energy and electron spectra in the absence and presence of coating materials were assessed in detail to provide insights into the alteration of radioenhancement efficacy. Additionally, *G*-values for common radiolytic species were

Table 1 Summary of the reviewed articles on the impact of nanoparticle coatings on the radiosensitization effect. (DTDTPA: diethylene-triaminepentaacetic acid; PEG: polyethyleneglycol, PVA: polyvinyl alcohol, AET: 2-aminoethanethiol, HAS: human serum albumin, AuNP: gold nanoparticle)

Study	Approach	Coating material and thickness	Key findings
Kong *et al.*[35]	Experiment: MTT assay on MCF-7 breast cancer cell lines	Glucose, cysteamine (AET)	More than one order of magnitude higher cellular uptakes for coated AuNPs Higher cytotoxicity and cell damage following X-ray irradiation for coated AuNPs
Xiao *et al.*[36]	Experiment: DSB induction in plasmid DNA	DTDTPA and DTDTPA:Gd (4 nm), thiolated undecane ($S–C_{11}H_{23}$) (2.5 nm)	Significant reduction in DNA strand breaks for coated AuNPs Notable decrease in radiosensitization for longer ligands (thicker coating layer)
Gilles *et al.*[30]	Experiment: agarose gel electrophoresis assay on pBlueScript plasmid DNA	PEG1000 (2.3 nm), PEG4000 (1.9 nm), PEG3500-NH2 (11.8 nm), PEG3500-COOH (9.3 nm), HSA (8.0 nm)	All coating materials had a negative impact on the generation of radicals and DNA damage The number of atoms in the coating can determine the reduction of hydroxyl radicals Certain chemicals within the coating, (*e.g.* thiols and alcohols) can scavenge the radicals
Spaas *et al.*[37]	Experiment: agarose gel electrophoresis assay on supercoiled plasmid DNA	PEG (4.1, 11.2, 14.3 nm)	Reduced radiosensitization effect for different dose ranges by increasing the thickness of the PEG layer
He and Chow[38]	Monte Carlo track structure simulation (Geant4-DNA)	Citrate, PEG, PVA	Coating layers do not affect the dose enhancement due to the low effective atomic number of the examined polymers (carbon, hydrogen, and oxygen), and thus, limited interactions with incident photons and secondary electrons
Koger and Kirbky[39]	Monte Carlo simulation (PENELOPE)	PEG (10 and 20 nm)	A 34% reduction of dose to the water surrounding the AuNP due to adding 20 nm of PEG Microscale simulations showed a 14% decrease in dose enhancement ratio for the same coating thickness The impact of a coating is more noticeable for smaller AuNPs, higher concentrations, and lower photon energies
Haume *et al.*[40]	Numerical simulation (MBN Explorer software)	PEG (1.4 nm)	A lower number of ligands attached to the AuNP surface results in higher yields of radical production Penetration of water molecules into the coating layer can enhance the number of free radicals Therefore, coatings with low density and high hydrophilic properties are the most efficient ones
Belousov *et al.*[41]	Monte Carlo simulation (Geant4)	PEG (8.5 nm)	Almost half of the produced electrons were absorbed by an 8.5 nm PEG layer The coating layer can increase the proportion of compton electrons in the electron spectra
Peukert *et al.*[42]	Monte Carlo track structure simulation (Geant4-DNA)	PEG (2, 5, 10, 15, 20 nm), silica (2, 5, 10, 15, 20 nm)	Adding the coating layer and increasing its thickness caused a significant decrease in dose and radiolysis enhancements

Table 1 (*Contd.*)

Study	Approach	Coating material and thickness	Key findings
			This is due to the absorption of secondary electrons and also a lower proportion of gold material in nanoparticles with thicker coatings, which decreased the yield of secondary electron generation per volume
Loscertales *et al.*[43]	Experiment: clonogenic assay on MDA-MB-231 breast cancer cells	PEG (7.6, 20.1 nm), citrate (7.5, 19.6 nm)	PEG-AuNPs showed enhanced production of singlet oxygen, but not hydroxyl, indicating that multiple reactive species contribute to radiosensitization PEG-AuNPs outperformed citrate-coated ones, with smaller AuNPs showing greater radiosensitization effects, consistent with ROS generation

quantified for each coating material, offering an understanding of the underlying chemical mechanisms.

Methodology

Generating the phase space files (PSFs)

To accurately model the radioenhancement behavior of gold nanorods, we employed a multiscale method consistent with existing literature,[57,66,67] utilizing the TOPAS code. Two phase space files (PSFs) were generated for the transition from a macroscale beam size to nanoscale simulations: (i) PSF1, recorded in a $10 \times 10 \times 1$ μm^3 water slab located 2 mm deep in a (1 cm)^3 water phantom, used to score the photons passing its surface; (ii) PSF2 on the coating surface, containing data for secondary electrons and photons escaping the coating surface, serving as the radiation source for subsequent chemistry simulations.

The simulations began with generating PSF1 using a 100 kVp X-ray beam with a 25 μm × 1 mm field size, designed to mimic a synchrotron microbeam. A kilovoltage photon beam was used in this study due to the significant role of photoelectron-based secondary electrons at this energy range, which is much less pronounced in megavoltage (MV) beams. This choice is also clinically relevant, as kV X-rays are commonly used for treating superficial tumors, including melanoma and other skin lesions.[68] To balance computation time and statistical uncertainty, in total 10^8 histories were used to generate this PSF, with the *g4em-standard_opt4* physics module being activated. The photon spectrum was produced using SpekPy v2.0 (ref. 69) with input parameters that included a 20° anode angle, a 0.8 mm Be filter, and a 3.9 mm Al filter. The PSF was then analyzed by extracting the photon spectrum, which was found to still be dominated by the primary photons. This photon spectrum was used for further simulations, and the resulting PSF1 was resized to a square of 160×160 nm^2 in the TOPAS input file to match the dimensions of the coated nanorod with a 50 nm-thick coating layer. The multiscale methodology applied here has been used in previous works,[15,23] where the radioenhancement properties of rod-shaped and sphere-shaped AuNPs were compared and the geometrical aspects of nanorods were optimized, such as size, orientation, and surface-area-to-volume ratio (SA:V). The approach used here and in previous work was validated against the results of a EURADOS exercise, an inter-comparison study on radioenhancement by gold nanoparticles under X-ray irradiation, which compared results from seven different TS codes modeling a single setup.[34,70–74] Adapting the beam size to the object under investigation (AuNR with coating) is suited for determining the additional contribution to absorbed dose and radiolytic yield from radiation interactions within this object.

A single AuNR, modeled as a cylinder with a diameter of 60 nm and a length of 180 nm (aspect ratio of 3), was positioned at the center of a (5 μm)^3 water cube and irradiated by the X-ray beam originating from PSF1. The size of the AuNR was sufficient to ensure a satisfactory number of interactions for secondary electron generation. The physics module *g4em-dna_opt7* was applied here, with a cutoff energy of 10 eV, and particle-induced X-ray emission (PIXE), the Auger effect, Auger cascades, and fluorescence radiation being activated. A schematic of the simulation geometry is shown in Fig. 1a. For the chemistry simulations, PSF2 was used as the radiation source, which is explained in the next section.

Impact of the coating layer

For the next stage, simulations were performed to compare the differences in energy deposition and emitted electron spectra from the AuNR coated by different materials. To model the nanorod coating, an ellipsoid covering the AuNR was used, presenting a shape almost similar to the actual nanoparticles.[75] By considering biocompatibility and frequency of use of coating materials reported in experimental investigations, four coating

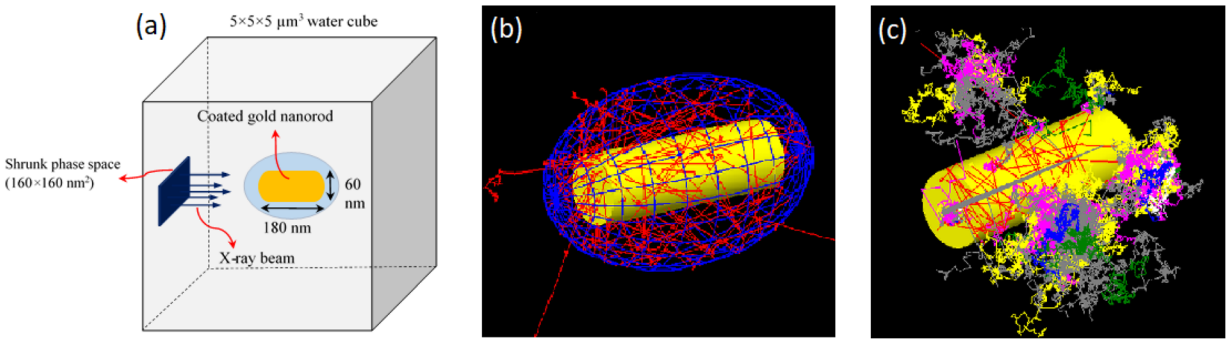

Fig. 1 Schematic view of simulation setup (a), tracks of secondary electrons (red lines) emitted from an AuNR within a 50 nm-thick coating layer (b), and tracks of chemical species generated around a non-coated AuNR (c). The images in (b) and (c) were obtained using TOPAS GUI with a low number of histories for illustration purposes only.

materials, namely silica, PEG, PEI, and CTAB, were selected and compared with the non-coated AuNR. Notably, CTAB is an ammonium-based surfactant essential in the synthesis of gold nanorods through the seed-mediated growth technique, where it primarily controls their growth and shaping.[76] Despite its well-known high cytotoxicity, CTAB is the primary coating layer after the synthesis of gold nanorods, therefore its impact on the radioenhancement efficiency cannot be ignored.[77]

The impact of coating thickness was also investigated by comparing 25 nm and 50 nm thicknesses. It is worth noting that, depending on the size and shape of the nanoparticles, the practical coating thickness is typically less than these values. For instance, PEG coatings might range from 2 nm to 15 nm.[30,78] However, the purpose of choosing these thicknesses was to highlight the influence of the coating layer. Furthermore, in practice, the coating layer may not uniformly cover the entire nanoparticle or have a consistent thickness. This is mainly due to the asymmetric geometry of nanorods and the inherent stochasticity of the synthesis and coating processes.[26] In our simulation, we modeled the coating as an ellipsoid enclosing the nanorod, with minor axes greater than the radius and half height of the cylinder by 25 and 50 nm for the two scenarios, respectively. For these cases, the distance between a point on the cylinder surface and the closest point on the ellipsoid surface varies between 3.6 nm and 25 nm and between 27.4 nm and 50 nm, respectively. Fig. 1b shows a gold nanorod embedded in a 50 nm-thick coating layer and examples of trajectories of secondary electrons emitted from this nanoparticle when photons (sampled from the 100 kVp X-ray spectrum) interact in the AuNR. Sample tracks of chemical species generated around a non-coated AuNR are also shown in Fig. 1c.

It is worth noting that in the simulation setup, only about 11% of the photons intersect the AuNR, and only about 0.4% of these undergo an interaction in the AuNR. The photons missing or traversing the AuNR without interaction may interact in the surrounding medium. These interactions contribute to the fluence of secondary electrons, to the overall dose distribution, and the production of ROS. However, since the photon interaction probability in the coatings can be assumed to be closer to that of water than that of gold. If it was identical to that of water, close to 80% of the photon interactions in the $(5\ \mu m)^3$ cube occurred within the AuNR. This implies that the difference in absorbed dose and ROS production with and without coating may have a bias in the order of 20% due to photon interactions in the water cube outside the AuNR. However, this bias can be expected to be roughly the same for all coatings and coating thicknesses.

Regarding the output parameters, the energy imparted per mass in the water cube outside the region occupied by the AuNR and its coating for different scenarios was measured. This quantity is the contribution of the irradiated volume containing the AuNR to the absorbed dose in this water cube and as a shorthand notation is referred to as dose. The measured doses were then normalized to the incident photon fluence to compare the behavior of nanoparticles with different coating layer thicknesses and materials. It is important to note that the lack of lateral CPE due to the micrometer size of our initial irradiation beam leads to an overestimation of the dose enhancement.[34,55,56] However, according to Thomas *et al.*,[79] under full backscattering conditions and lateral CPE, the local dose enhancement aligns closely with the results reported in the EURADOS exercise,[74] which used a confined beam. This indicates that neglecting the Compton scattered photon field introduces negligible bias and simulations under full backscattering conditions would lead to similar results. Accordingly, the study's objective of comparing various coating materials could be achieved by comparing the contributions of the irradiated volume to the dose and the yield of radiolytic products.

The electron fluence spectra in the water volume outside the AuNR and its coating were also acquired to assess how different coatings could affect the production and absorption of secondary electrons. In particular, electron fluence was scored in the whole water cube (outside the AuNR with coating) and, in addition, in a spherical shell with 150 nm inner radius and 500 nm outer radius. The electron spectrum in the TOPAS code output file is presented as electron fluence (electrons per mm^2) for each energy bin. These fluence values were divided by the bin width to obtain the spectral energy fluence $\varphi(E)$ (in mm^{-2} keV^{-1}) and then normalized to the fluence of photons hitting the AuNR surface (photons per mm^2). For plotting the frequency

density of emitted electrons per logarithmic energy intervals on the *X*-axis, the electron fluence in each energy bin was multiplied by the average energy of the bin. This approach, previously employed by Rabus *et al.*,[73] helps highlight the contribution of different energy ranges to the overall particle fluence. To facilitate quantitative comparisons, integrals of electron fluence per incident photon fluence (Ψ_e) were also calculated for three different electron energy ranges: below 3.5 keV (primarily associated with Au M-shell Auger-Meitner electrons, Coster-Kronig electrons, and low-energy secondary electrons), between 3.5 and 15 keV (mainly related to Au L-shell Auger-Meitner electrons), and above 15 keV (mostly photoelectrons). The following equation was used for integrating the electron fluence over the energy:

$$\Psi_e = \frac{1}{\Phi_p}\int_{E_1}^{E_2}\varphi(E)\mathrm{d}E \quad (1)$$

where $\varphi(E)$ is the spectral fluence of emitted electrons with energy E, and φ_p is the fluence of incident photons, and E_1 and E_2 are the lower and upper bounds of the respective energy interval. Analyzing these output parameters could provide a comprehensive evaluation of the influence of coating material on the radioenhancement efficiency of gold nanorods.

In addition to the described physical parameters, we investigated the chemical phase of the radiolysis process following X-ray irradiation in the presence of AuNR using the TOPAS-nBio extension.[52,59,80] The chemical reactions of radiolytic products were modelled using the *TsEmDNAChemistry* module.[52,60,81] We calculated the *G*-values (the number of molecules produced or consumed per 100 eV of absorbed radiation energy) using the independent reaction time (IRT) method, which provides computational advantages compared to the conventional Step-by-Step (SBS) method.[65,82] Further details on these simulation methods are available in the referenced studies.

To ensure the reliability of our simulation model, a validation study was conducted by reproducing the work of Rudek *et al.*,[83] specifically focusing on radiolysis yields in pure water (without nanoparticles). Following their setup, a spherical cell (9 μm in diameter) was modelled containing a spherical nucleus (5.4 μm in diameter) within a $(12\ \mu m)^3$ water cube. A 50 keV photon beam of $9 \times 9\ \mu m^2$ was directed at the cell from a distance of 1.5 μm from the cell surface. We measured *G*-values for seven radiolytic species in the cytoplasm: hydrogen peroxide (H_2O_2), hydronium ion (H_3O^+), hydrogen atom ($H^\bullet$), dihydrogen molecule (H_2), hydroxide (OH^-), hydroxyl radical ($^\bullet OH$), and solvated electron (e_{aq}^-). Measurements were taken at 20 logarithmic time steps from 1 ps to 1 μs, corresponding to the chemical stage of water radiolysis. The diffusion coefficients and reaction rates were precisely set according to the referenced study.[52,83]

After validation, the main simulations used the PSF2 from the coating surface as the particle source, positioned at the center of a $(5\ \mu m)^3$ water cube. The impact of the coating on *G*-values was assessed by comparing the yields of chemical species with and without the presence of the coating layer. Measurements were conducted within the water cube (excluding the AuNR and coating regions), again at 20 logarithmic time steps from 1 ps to 1 μs, and results were reported for the above radiolytic mentioned species. The track-structure and chemistry simulations performed using TOPAS (v3.9) and TOPAS-nBio (v2.0) are currently limited to liquid water, gold, nitrogen gas, and four DNA-substitute materials (tetrahydrofuran, trimethyl phosphate, purine, and pyrimidine).[84] For materials outside this set (including the coating materials used in this work), the code automatically applies the Livermore physics model. Thus, the Geant4-DNA physics list (g4em-dna_opt7) is used by default to handle electron transport in water and electron–gold interactions.[85–87] This approach was applied in our previous works and benchmarked against existing literature.[23]

Following the approach taken by Geant4, TOPAS employs a range-based cut system to handle production thresholds dynamically, depending on particle type, energy, material properties, and range cuts. Rather than setting a fixed energy threshold, the cut in range is converted into a kinetic energy threshold for each material based on its stopping power and geometry.[58,88] Our simulations used the default energy thresholds of 100 eV for general electromagnetic interactions (Livermore) and 10 eV for Geant4-DNA models. These default values serve as the basis for converting to the appropriate particle step size for each material. While these settings ensure accurate track-structure modeling for comparing various coating materials, prior studies have demonstrated that step size, range cuts, and the choice of physics models can introduce uncertainties at the nanoscale.[89–91] Nevertheless, these factors should be considered when interpreting absolute dose values in nanoparticle-enhanced radiotherapy.

The simulations were performed on a PC with a 2.7 GHz Intel Core i5-7500T CPU and 16 GB of RAM, running Linux Ubuntu within the Windows Subsystem for Linux (WSL). The simulations of chemical reactions were conducted using 10^6 histories.

Results

Impact of coating material on physical interactions

The physical characteristics of the four examined coating materials are listed in Table 2, comparing the effective atomic number (Z_{eff}), density, and molecular weight of the examined coating materials. The Z_{eff} values were determined using the Mayneord equation,[92] following the methodology outlined by Nawi *et al.*:[93]

$$Z_{eff} = \left(\sum_i a_i \times Z_i^{2.94}\right)^{\frac{1}{2.94}} \quad (2)$$

where a_i is the fractional contributions of the ith element to the overall electron count of the molecule, and Z_i is the atomic number of the associate element.

The dose values within the water cube normalized to the incident photon fluence (in Gy nm^2) for the four coating materials with thicknesses of 25 nm and 50 nm are also presented in Fig. 2. The relative uncertainty associated with this data set is less than 1%.

Table 2 Physical characteristics of coating materials (Z_{eff} = effective atomic number)

Material	Structural formula	Density (g cm^{-3})	Molecular weight (g mol^{-1})	Z_{eff}
Cetyltrimethylammonium bromide (CTAB)	$C_{19}H_{42}BrN$	0.50	364.5	19.5
Polyethylene glycol (PEG)	$C_{2n}H_{4n+2}O_{n+1}$	1.12	62.1	6.6
Polyethyleneimine (PEI)	$(C_2H_5N)_n$	1.03	43.1	5.9
Silica	SiO_2	2.32	60.1	11.6
Water	H_2O	1.00	18.0	7.4

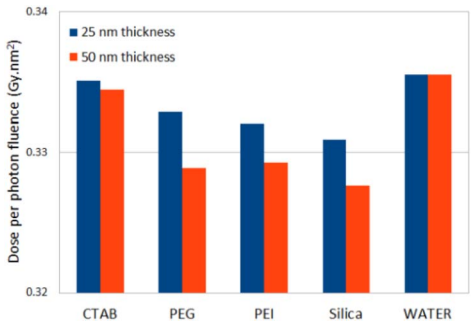

Fig. 2 Dose normalized to incident photon fluence for different coating materials with 25 nm and 50 nm thicknesses.

Fig. 3a presents the electron spectra sampled in a spherical shell of 150 nm inner radius and 500 nm outer radius for an AuNR with two different silica coating thicknesses, as well as for an uncoated AuNR. The electron fluence spectra within the water cube for the same nanoparticles are shown in Fig. 3b. The *y*-axis here represents the spectral fluence of electrons per incident photon fluence, multiplied by the energy, as explained in the methodology section. Silica was chosen as a sample material to illustrate the variation between different scenarios. However, the differences in electron spectra among the four coating materials were negligible due to the comparable characteristics of the four coating materials examined.

In the energy range of M-shell Auger-Meitner electrons (500 eV to 3.5 keV), the electron spectra in the water shell (Fig. 3a) exhibit a distinct trend in contrast to those in the water cube (Fig. 3b).

Table 3 summarizes the integral of electron fluence normalized by the fluence of incident photons. The data for three energy ranges, two thicknesses, and four coating materials as well as AuNR with no coating are presented. The uncertainty for this set of data is between 1% to 2% according to the electron frequencies in different energy bins.

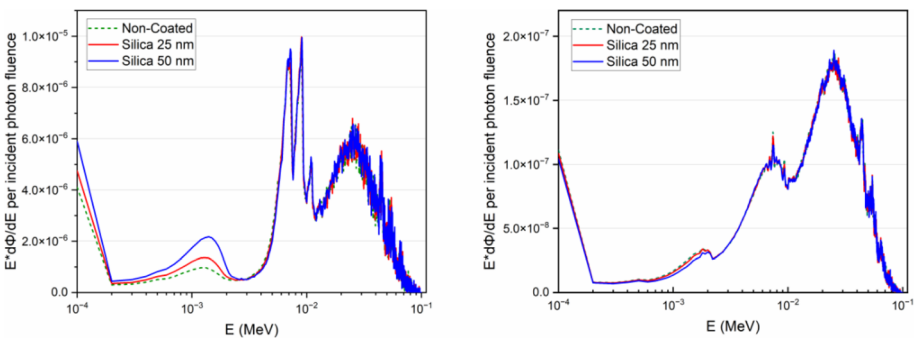

Fig. 3 Fluence spectra of (a) the emitted electrons, and (b) the electrons in the water cube.

Table 3 The integral of electron fluence per incident photon fluence (Ψ_e) in the water cube for AuNR coated with different materials and thicknesses, compared to the non-coated nanorod. The uncertainty for the values is between 1% to 2%

		The integral of electron fluence per incident photon fluence ($\times 10^{-7}$)				
Energy range (keV)	Coating thickness (nm)	CTAB	PEG	PEI	Silica	Non-coated
0–3.5	25	1.68	1.66	1.66	1.66	1.70
	50	1.63	1.57	1.57	1.58	1.70
3.5–15	25	1.30	1.28	1.28	1.28	1.28
	50	1.35	1.27	1.27	1.28	1.28
15–100	25	1.90	1.88	1.88	1.89	1.89
	50	1.94	1.86	1.86	1.90	1.89

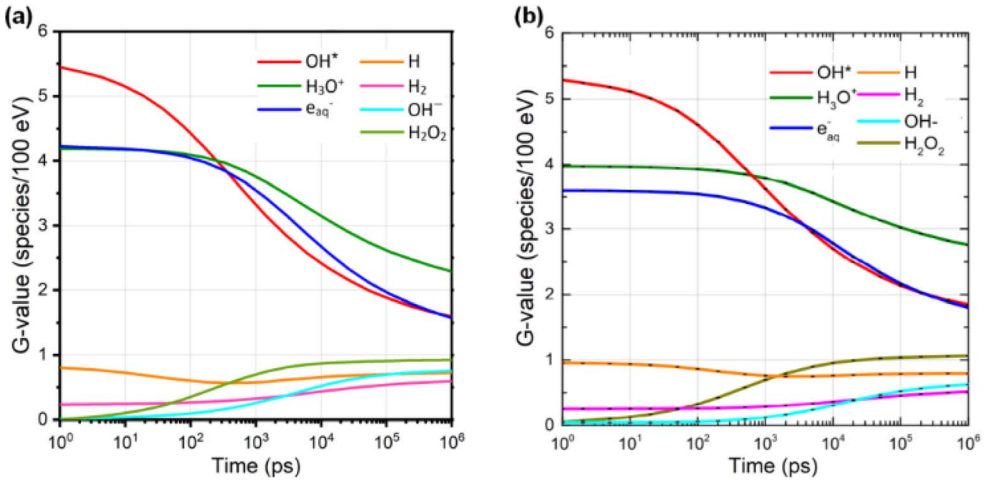

Fig. 4 *G*-values for radiolytic species from (a) the present work, and (b) the Rudek *et al.*[83] study, reproduced with permission.

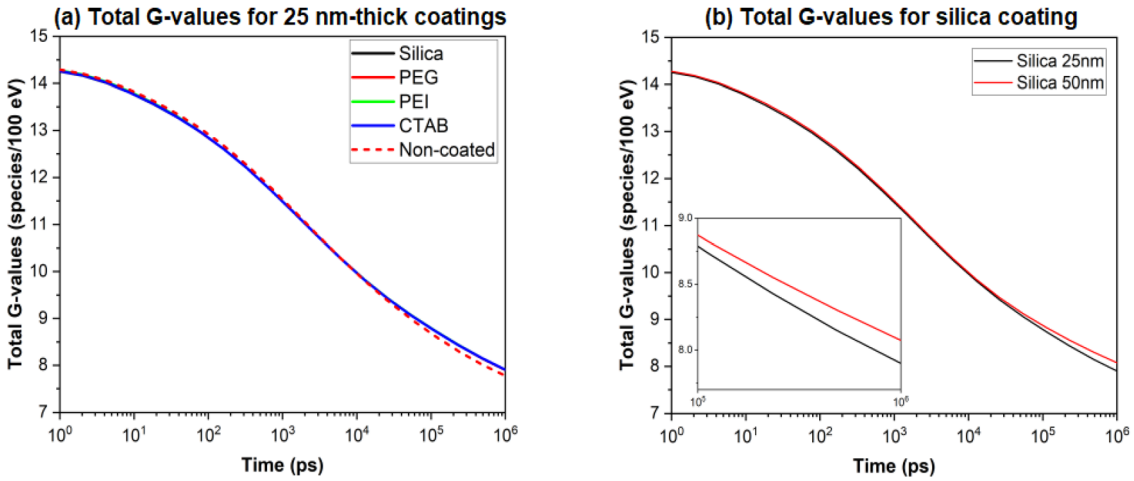

Fig. 5 Total *G*-values for different coatings with 50 nm thickness (a), and silica coating with two thicknesses (b). The inset in (b) provides a magnified view of the time interval from 100 ns to 1 μs.

Impact of coating material on the generation of chemical species

Fig. 4a presents the *G*-values from our validation simulations compared to previously published data from Rudek *et al.*[83] as shown in Fig. 4b. Our results have slight differences in *G*-values, which can be attributed to variations in the chemistry modules, particularly in the reactions of the pre-chemical stage. A detailed description of these differences will be provided in the Discussion section.

The total *G*-values for all the coating materials (with 25 nm thickness) compared with AuNR with no coating are shown in Fig. 5a. The *Y*-axis in this graph is the sum of all seven chemical species at each specified time. As observed, the *G*-values in this graph show almost no distinctions between different coatings. Accordingly, Fig. 5b presents the total *G*-values for silica coating with two thicknesses, with the inset providing a zoomed-in plot from the original graph, illustrating the time interval of 100 ns to 1 μs more clearly.

The *G*-values of all chemical species for both non-coated and silica-coated AuNRs at 1 μs post-irradiation are listed in Table 4. The data show an increasing trend in *G*-values for the two key radiolytic species, hydroxyl radical (˙OH) and solvated electron (e_{aq}^-), with the addition of a coating layer and as its thickness increases.

Table 4 The *G*-values of produced chemical species for non-coated and silica-coated AuNR at 1 μs after the irradiation

Coating thickness (nm)	*G*-values (#/100 eV energy deposition)							
	H_2O_2	H_3O^+	H˙	H_2	OH^-	˙OH	e_{aq}^-	SUM
0	0.76	1.84	0.65	0.65	0.69	1.57	1.60	7.78
25	0.75	1.82	0.67	0.67	0.73	1.60	1.66	7.90
50	0.75	1.92	0.67	0.64	0.69	1.67	1.73	8.07

Discussions

With this study, we investigated the relationship between the properties of the coating layer and the radioenhancement efficacy of gold nanorods under 100 kVp X-ray irradiation. Using the TOPAS code, we explored the impact of four coating materials and their thicknesses on the absorbed dose, emitted electron spectrum, and the generation of radiolytic species. As illustrated in Fig. 2, adding the coating layer and increasing its thickness decreases the dose contribution due to the AuNR within the water phantom up to 7% ± 1% across the examined materials. Considering the data presented in Table 2, no meaningful correlation could be found between the dose and the density, molecular weight, or effective atomic numbers of the examined materials. Regarding CTAB, the presence of bromine ($Z = 35$, K-edge energy = 13.47 keV) in its structure can likely generate extra photoelectrons and contribute to Compton scattering upon X-ray irradiation. These interactions could counteract the electron absorption effect since electrons produced in the coating increase the emitted electron fluence from the coated nanorod.

The 50 nm layer displayed higher electron absorption, leading to a greater decrease in dose across all materials. This is qualitatively in agreement with the experimental findings of Spaas *et al.*[37] and Gilles *et al.*,[30] indicating a consistent trend in the impact of coating layers on dose enhancement. These two studies showed that increases in PEG thickness (longer ligands) could effectively decrease the radioenhancement efficiency. However, the dose reduction observed in our study was not as high as the decrease in radioenhancement reported in these experiments. Since the average product of photon energy and mass-energy absorption coefficient of water for a 100 kVp photon spectrum is in the order of 40 Gy nm^2, the dose-to-fluence ratio under CPE would be of this order of magnitude so that the changes imposed by the coating layers would be even smaller. It is also worth noting that the use of air as the material in the "World" region may have further disrupted the CPE condition and become a potential caveat in the DER measurements. This difference between our findings and the experimentally observed reduction of radioenhancement cannot be only attributed to simplifications and assumptions made in our simulations, such as modeling a single nanoparticle, predefining the nanorod's orientation, and assuming a uniform coating thickness. On the contrary, this discrepancy suggests a significant influence on the chemical reactivity and scavenging properties of the coating layers.

The result reported in Fig. 2 also shows qualitative agreement with the findings of He and Chow,[38] where the difference in dose enhancement with the addition of a coating layer was undetectable within the first decimal value. However, slight differences emerge upon more precise examination due to the multiple physical differences between the examined materials. While this referenced study did not specify the thickness of the coating layers, our findings suggest that variations in coating material and thickness can influence the dose values, even though to a minor extent. Additionally, the observed dose enhancement was confirmed to be highly dependent on the scoring regions employed in the simulations.[94,95] While we have measured the dose within a water cube containing the AuNR, He and Chow's study assessed the dose in a DNA molecule located at different distances from the nanoparticle (30 to 130 nm), resulting in no visible variations in results with and without coating.

Our findings also align with Peukert *et al.*,[42] where a multiscale approach was taken to measure the dose and radiolysis enhancements for proton therapy. Concerning the coating material, Peukert *et al.* observed a significant decrease in enhancement factors with the addition of coating and increasing its thickness from 2 to 20 nm. Despite the inherent differences between our approach and theirs, such as variant irradiation type and simulation geometry, it seems feasible to draw general conclusions regarding the absorption of low-energy electrons by various coatings. However, conducting detailed quantitative comparisons on dose and radiolysis enhancement is challenging. One potential source of bias in the study of Peukert *et al.*, which has led to notably high enhancement factors, is the beam size. As acknowledged by the authors, the lack of CPE due to using a confined proton beam could raise the enhancement factors by underestimating the impact of the initial beam on energy deposition. Moreover, the beam size in their study was equal to the size of the AuNP plus coating, resulting in varying beam sizes for different coating thicknesses. This could potentially affect the enhancements by altering the number of particles entering the AuNP and also the deposited energy in the absence of nanoparticles. Therefore, it is presumed that correcting these biases would significantly reduce the enhancement factors and moderate the difference between various coating thicknesses.

Fig. 3a shows the effect of the coating layer on secondary electrons that are emitted from both non-coated and silica-coated AuNRs and transported within a 150–500 nm water shell. The electron spectra are significantly reduced in the energy range between 0 and 3 keV compared to studies reporting the energy spectra escaping the AuNR,[23] since these electrons are absorbed within the first 150 nm from the AuNR surface.[73] The higher fluence of emitted M-shell Auger-Meitner electrons in the presence of the coating layer was unexpected. One possible explanation is the use of different physics lists and hence different simulations of electron transport for different materials. As previously mentioned, the physics module inside the coating material is Livermore, while in the non-coated scenario, where the coating is replaced with water, the *g4em-dna_opt7* physics module is applied in the same region. This difference could potentially account for the observed discrepancy. The fluence spectra of electrons in the water cube are shown in Fig. 3b, revealing an almost one order of magnitude decrease compared to the electrons in the spherical shell in the vicinity of the AuNR. This is mainly because the electrons predominantly originate in the AuNR and the cube has a larger mean cross-sectional area than the spherical shell. The change in the spectral shape of these spectra compared with the spherical shell is due to the energy loss of lower energy electrons in the larger water medium. The M-shell electrons show

a slightly higher abundance in the non-coated AuNR here, which is explained by the fact that the scoring volume encompasses the region near the coating surface. Similar results were observed for the other materials assessed, although their spectra are not included in this figure. While the differences between the scenarios are particularly observable in the low-energy part of the spectra, drawing definitive conclusions based solely on the spectra is challenging.

Nonetheless, the data presented in Table 3 suggest that the coating materials mostly affect electrons up to 3.5 keV energy range. As mentioned, these electrons predominantly include Auger-Meitner electrons from the M-shells and Coster-Kronig electrons of the L-shells of the gold atom, which typically have energies below 2 keV.[96,97] The average reduction in the integrated frequency density of these low-energy electrons was about 8% and happened for 50 nm thickness. The data also indicate that the number of electrons in the 3.5 to 100 keV energy range is only minimally affected by the coating. The results from the electron spectra analysis are consistent with the dose measurements, emphasizing the predominant role of low-energy secondary electrons originating in the AuNR in the local physical dose enhancement around it. While the typically low effective atomic numbers of the elements contained in the examined coating materials could explain the small electron absorption percentages, further investigation could determine a coating material and thickness or combinations of the two that would be optimal in terms of physical interactions.

For validation of the chemistry simulations using TOPAS-nBio, water radiolysis simulation results were compared with those reported by Rudek *et al.*[83] (Fig. 4). The comparison reveals minor differences in the *G*-values of the initially dominant species ($^{\bullet}OH$, H_3O^+, and e_{aq}^-), which subsequently influence the *G*-values of less prominent species. These variations are most likely attributable to differences in the pre-chemical reaction models implemented in different versions of the code, as the same chemical reactions and diffusion rates were used in the referenced studies.[60,98] For example, the lower *G*-values of $H^{\bullet}$ and H_2O_2 observed in the present results are likely associated with the initially greater concentration of e_{aq}^-, a highly reactive reductive scavenger of both $H^{\bullet}$ and H_2O_2. Despite these differences, the temporal trends in the *G*-values (from 1 ps to 1 μs) show general qualitative agreement with those reported by Rudek *et al.*

Additionally, the material balance among the species was evaluated using the equations provided by:[52]

$$G_{ox} = G_{\cdot OH} + 2G_{H_2O_2} = G_{-H_2O} \quad (3)$$

$$G_{red} = G_{e_{aq}^-} + 2G_{H_2} + G_{H^{\cdot}} = G_{-H_2O} \quad (4)$$

Accordingly, the G_{ox}/G_{red} ratio in our simulations is between 0.987 to 0.992 at different times, showing that the loss of species due to their diffusion outside the volume had a negligible effect on the balance of species inside.

Fig. 5a shows the total *G*-values for all coating materials with a 50 nm thickness, revealing a difference between coated and non-coated nanorods, but no discernible difference among the various coating materials. This outcome was not unexpected after observing the slight differences in dose and electron spectra between these materials. One limitation of the tools used in this study was that the available versions of TOPAS-nBio and Geant4-DNA can only model chemical reactions in pure liquid water. Consequently, the generation and scavenging of ROS at the interface of the AuNP with the coating layer, and within the coating material itself, cannot be modeled. Although the code can simulate the scavenging reactions of chemical species,[99] the scavenging properties of the studied coating materials are not implemented. TOPAS-nBio and Geant4-DNA use the Brownian dynamics and the Smoluchowski theory of diffusion to model the diffusion of reactive species.[54,100] According to this theory, molecules diffuse from areas of higher concentration to areas of lower concentration along the concentration gradients with specific diffusion coefficients. Given that there is a higher density of energy deposits near nanoparticle,[101] the ensuing density gradient will drive ROS away from the nanoparticle. Furthermore, while inter-track reactions impact the scavenging of free radicals and could have been modelled by TOPAS, we did not include this effect in our simulations as it is insignificant for radiations with a linear energy transfer (LET) lower than 2 keV μm^{-1} (ref. 62 and 102) and we are not considering FLASH conditions. From the mass-energy absorption coefficients of water, it can be estimated that a dose rate of 2 Gy min^{-1} corresponds to a photon fluence rate of about 7×10^{10} cm^{-2} s^{-1}. For a uniform extended photon beam, such a fluence rate results in interaction rates of about 8×10^{-3} s^{-1} in the AuNP and 14 s^{-1} in the $(5\ \mu m)^3$ water cube, or 8×10^{-9} and 1.4×10^{-5} interactions per μs. Therefore, the probability of simultaneous occurrence of more than one photon interactions in the AuNP or of one photon interaction in the AuNP and one in the water cube is negligibly small, and neglecting inter-track reactions appears justified.

The data presented in Fig. 5b reveals a non-negligible difference in total *G*-values when comparing the two thicknesses of the coating layer. Based on the dose values and integrated electron frequencies, it could be expected that adding the coating layer would decrease ROS production. Interestingly, however, the *G*-values for the 50 nm-thick coating were slightly higher than those for the 25 nm coating. This distinction, evident in Fig. 5b and the inset, starts at *ca.* 10 ns post-irradiation and becomes more noticeable over time. This effect was also observed in a recent study by Mansouri *et al.*,[103] where adding the coating layer increased the radiolysis enhancement fraction for metal nanoparticles under 100 keV X-ray irradiation.

One explanation for this unexpected observation could be the generation of small clusters of reactive species known as irradiation-induced "spurs".[104] The concentration of chemical species around the path of electrons traversing water is significantly high. This, in turn, can result in high probabilities of intra-spur recombination between the free radicals (mainly $H^{\bullet}$, $^{\bullet}OH$, and e_{aq}^-), which will reduce their quantity and thus the likelihood of cell damage. On the other hand, the addition of a coating layer slightly increases the E_{mean} of electrons due to the elimination of low-energy electrons. According to the Bethe-

Bloch approximation, for electrons with energies between 10 keV and 1 MeV, the stopping power (and thus the LET) in liquid water decreases as the energy increases.[105] Hence, adding a coating layer marginally elevates the E_{mean} and decreases the LET, which could lead to a reduced concentration of free radicals in spurs and subsequently lower the likelihood of recombination.[106,107] Consequently, the decrease in recombination and the resulting increase in the number of surviving species could lead to higher *G*-values for coated AuNRs beyond the 10 ns timeframe. This trend is also reflected in Table 4, where the impact of the coating layer is more pronounced for $^{\bullet}OH$, and e_{aq}^{-} at the end of the chemical stage (1 μs). This finding suggests that the relationship between coating thickness and the generation of radiolytic species is more complex than initially anticipated, demanding further investigation.

In summary, while the loss of low-energy electrons within the coating layer seems inevitable, its impact on the predicted radioenhancement efficiency appears to be less significant than previously reported in the literature.[30,37,42] The slight increase in total *G*-values also suggests a potential, previously unforeseen benefit of enhancing efficiency by the addition of a thick coating layer. Our findings indicate that, from the physics perspective, there is minimal distinction between investigated coating materials regarding secondary electron emission, dose deposition, and ROS generation. This appears to be aligned with the results from a recent simulation study of ROS production around an irradiated gold sphere under CPE conditions indicating only sub-percentage enhancement.[108] Nevertheless, from the chemical aspect, it is important to acknowledge that many chemical reactions and their reaction rate constants remain unknown or reported with conflicting values in the literature, making a truly comprehensive assessment of these reactions challenging at present. Therefore, experimental studies and practical applications should also consider factors such as the chemical and biological interactions of coated nanoparticles with the bioenvironment, the availability of coating materials, and the cost-effectiveness and sustainability of their synthesis. Our findings also highlight the need for further research to better understand the complex effects of coating layers on these aspects.

As mentioned, a key limitation of this study is that the simulations model radiolysis in pure liquid water, without considering chemical and biological scavenging effects that could influence ROS dynamics. Additionally, the single-nanoparticle approach does not account for potential clustering or realistic NP distribution in biological environments, which can affect dose enhancement and secondary electron interactions.

Conclusion

The characteristics of nanoparticles, including material, shape, size, and surface coating, are crucial in determining the efficacy of the radioenhancement process. Specifically, the coating layer can influence the efficiency of the emitted secondary electrons and also interactions with the cellular environment. Despite its importance, there is a research gap in the literature regarding a comprehensive exploration of various coating materials and their specific effects on secondary electron spectra and radiolysis products.

To address this gap, we conducted simulations using the TOPAS MC code and the TOPAS-nBio extension. Our investigation focused on evaluating how different coating materials and thicknesses affect dose deposition, secondary electron emission, and the generation of radiolytic species. Four coating materials (silica, PEG, PEI, and CTAB) at two thicknesses (25 and 50 nm) were explored. The results showed a reduction in dose contribution from the presence of the AuNR ranging from 1% to 7% across all examined materials and thicknesses, with CTAB coating exhibiting the lowest decrease. Additionally, we observed comparable decreases in the integrated frequency density of low-energy electrons ($E < 3.5$ keV) for all materials. In contrast, the remainder of the electron spectra was only minimally impacted by the coating layer.

Accordingly, our simulation for the chemistry stage of the radiolysis process also demonstrated consistent total *G*-values across various coating materials. An interesting observation is that the increase of coating layer thickness could slightly increase the total *G*-values after about 10 ns after a photon interaction occurred. This phenomenon can be attributed to the removal of low-energy electrons, increasing mean energy, and a subsequent reduction in LET. This decrease in LET leads to lower concentrations of radiolytic species and reduced recombination of free radicals within radiation-induced spurs, potentially resulting in an increased quantity of these radicals over longer durations.

Our findings generally align with existing literature that reports a decrease in radioenhancement due to the presence of a coating layer. However, the simplifications and assumptions made in this study, along with the lack of accurate experimental data on the scavenging properties of certain coating materials, have made precise quantitative comparisons with available experimental data challenging. Nevertheless, our results suggest that while the coating layer negatively affects the physical radiation effects of nanoparticles, this impact may not be as substantial to account for the magnitude of changes in radioenhancement efficiency from coating layers previously reported in the literature. Additionally, we observed a potential benefit of the coating layer in slightly increasing the number of radiolytic species, highlighting the need for further simulation and experimental investigations into the chemical impacts.

Overall, this study suggests that concerns about negative physical influences through the absorption of secondary electrons might be overstated in the literature. While other physical phenomena besides dose are also involved in nanoparticle radioenhancement,[109] it appears that the optimal coating material should primarily be determined by contributing chemical and biological parameters. These include the accessibility of materials, the coating procedure, the stability and biocompatibility of the coating, and its potential for implementing targeted delivery. Additionally, the interaction of the coating material with the biological environment should be considered. Future research could focus on examining how water molecules penetrate coating layers and influence ROS

generation, as well as exploring the scavenging properties of these layers. The impact of nanoparticle clustering on the radioenhancement efficiency could also be investigated. Future work may also include experimental validation to further benchmark our simulation results. Advancing such studies will rely on the continued development of simulation tools and the expansion of their chemical reaction datasets.

Data availability

Data for this article, including the TOPAS input files and output files, are available from the GitHub repository at **https://github.com/Alitmedical/TOPAS-files.git**. A DOI for this dataset is available *via* Zenodo at **https://doi.org/10.5281/zenodo.14916706**. The Monte Carlo simulation code employed in this work is TOPAS MC v.3.9 (available at **https://www.topasmc.org** and **https://github.com/topasmc/topas-docs.git**) and its TOPAS-nBio extension v.1.0 (available at **https://github.com/topas-nbio/TOPAS-nBio-regression.git**). Graphical representations were generated using Origin software v.2024 (**https://www.originlab.com/**).

Author contributions

A. T: writing – original draft, writing – review & editing, visualization, validation, software, methodology, formal analysis, data curation, conceptualization. M. U. K: writing – review & editing, supervision, project administration, conceptualization. H. R: writing – review & editing, validation, supervision, methodology, formal analysis, data curation, conceptualization. F. M: writing – review & editing, methodology, formal analysis. D. A. B: writing – review & editing, supervision, formal analysis, conceptualization.

Conflicts of interest

There are no conflicts to declare.

Acknowledgements

The Sunway University studentship award for A. T. is acknowledged.

References

1 K. Wang and J. E. Tepper, *CA Cancer J. Clin.*, 2021, **71**, 437–454.
2 S. C. Freitas, D. Sanderson, S. Caspani, R. Magalhães, B. Cortés-Llanos, A. Granja, S. Reis, J. H. Belo, J. Azevedo, M. V. Gómez-Gaviro and C. T. de Sousa, *Cancers*, 2023, **15**, 383.
3 Y. Gao, R. Liu, C. W. Chang, S. Charyyev, J. Zhou, J. D. Bradley, T. Liu and X. Yang, *J. Appl. Clin. Med. Phys.*, 2022, **23**, 1–22.
4 Q. Li, L. Hang, W. Jiang, J. Dou, L. Xiao, X. Tang, Y. Yao and Y. Wang, *Biomaterials*, 2020, **257**, 120235.
5 I. Kempson, *Int. J. Mol. Sci.*, 2022, **21**, 9–11.
6 Z. Cheng, M. Li, R. Dey and Y. Chen, *J. Hematol. Oncol.*, 2021, **14**, 1–27.
7 J. C. L. Chow, in *Nanostructures for Cancer Therapy*, Elsevier Inc., 2017, vol. 2030, pp. 383–403.
8 D. F. Regulla, L. B. Hieber and M. Seidenbusch, *Radiat. Res.*, 1998, **150**, 92–100.
9 A. Subiel, R. Ashmore and G. Schettino, *Theranostics*, 2016, **6**, 1651–1671.
10 I. Kempson, *Wiley Interdiscip. Rev.:Nanomed. Nanobiotechnol.*, 2021, **13**, 1–19.
11 S. Lacombe, E. Porcel and E. Scifoni, *Cancer Nanotechnol.*, 2017, **8**, 9.
12 Y. Zhang, X. Han, Y. Liu, S. Wang, X. Han and C. Cheng, *Mater. Adv.*, 2022, **3**, 3709–3725.
13 S. Rosa, C. Connolly, G. Schettino, K. T. Butterworth and K. M. Prise, *Cancer Nanotechnol.*, 2017, **8**, 1–25.
14 H. Shen, H. Huang and Z. Jiang, *Front. Pharmacol*, 2023, **14**, 1–7.
15 A. Taheri, M. U. Khandaker, H. Rabus, F. Moradi and D. A. Bradley, *Radiat. Phys. Chem.*, 2025, **230**, 112589.
16 J. C. L. Chow, *AIMS Biophys.*, 2024, **11**, 340–369.
17 J. F. Hainfeld, D. N. Slatkin and H. M. Smilowitz, *Phys. Med. Biol.*, 2004, **49**, N309.
18 I. Hammami, N. M. Alabdallah, A. Al Jomaa and M. Kamoun, *J. King Saud Univ., Sci.*, 2021, **33**, 101560.
19 S. Alex and A. Tiwari, *J. Nanosci. Nanotechnol.*, 2015, **15**, 1869–1894.
20 S. Penninckx, A. C. Heuskin, C. Michiels and S. Lucas, *Cancers*, 2020, **12**, 1–361.
21 K. Nejati, M. Dadashpour, T. Gharibi, H. Mellatyar and A. Akbarzadeh, *J. Cluster Sci.*, 2022, **33**, 1–16.
22 A. Taheri, M. U. Khandaker, F. Moradi and D. A. Bradley, *Radiat. Phys. Chem.*, 2023, **212**, 111146.
23 A. Taheri, M. U. Khandaker, F. Moradi and D. A. Bradley, *Phys. Med. Biol.*, 2024, **69**, 045029.
24 E. Mansouri, A. Mesbahi, H. Hamishehkar, S. Montazersaheb, V. Hosseini and S. Rajabpour, *BMC Chem.*, 2023, **17**, 180.
25 D. Howard, S. Sebastian, Q. V. C. Le, B. Thierry and I. Kempson, *Int. J. Mol. Sci.*, 2020, **21**, 579.
26 P. Del Pino, F. Yang, B. Pelaz, Q. Zhang, K. Kantner, R. Hartmann, N. Martinez De Baroja, M. Gallego, M. Möller, B. B. Manshian, S. J. Soenen, R. Riedel, N. Hampp and W. J. Parak, *Angew. Chem., Int. Ed.*, 2016, **55**, 5483–5487.
27 K. Haume, S. Rosa, S. Grellet, M. A. Śmiałek, K. T. Butterworth, A. V. Solov'yov, K. M. Prise, J. Golding and N. J. Mason, *Cancer Nanotechnol.*, 2016, **7**, 1–20.
28 I. Fratoddi, I. Venditti, C. Cametti and M. V. Russo, *Nano Res.*, 2015, **8**, 1771–1799.
29 R. Zhang, F. Kiessling, T. Lammers and R. M. Pallares, *Drug Delivery Transl. Res.*, 2023, **13**, 378–385.
30 M. Gilles, E. Brun and C. Sicard-roselli, *Colloids Surf., B*, 2014, **123**, 770–777.
31 J. Tournebize, A. Boudier, O. Joubert, H. Eidi, G. Bartosz, P. Maincent, P. Leroy and A. Sapin-Minet, *Int. J. Pharm.*, 2012, **438**, 107–116.

32 L. Digiacomo, S. Palchetti, F. Giulimondi, D. Pozzi, R. Z. Chiozzi, A. L. Capriotti, A. Laganà and G. Caracciolo, *Lab Chip*, 2019, **19**, 2557–2567.
33 X. D. Zhang, D. Wu, X. Shen, J. Chen, Y. M. Sun, P. X. Liu and X. J. Liang, *Biomaterials*, 2012, **33**, 6408–6419.
34 H. Rabus, W. B. Li, C. Villagrasa, J. Schuemann, P. A. Hepperle, L. de la Fuente Rosales, M. Beuve, S. Di Maria, A. P. Klapproth, C. Y. Li, F. Poignant, B. Rudek and H. Nettelbeck, *Phys. Medica*, 2021, **84**, 241–253.
35 T. Kong, J. Zeng, X. Wang, X. Yang, J. Yang, S. McQuarrie, A. McEwan, W. Roa, J. Chen and J. Z. Xing, *Small*, 2008, **4**, 1537–1543.
36 F. Xiao, Y. Zheng, P. Cloutier, Y. He and D. Hunting, *Nanotechnology*, 2011, **22**, 465101.
37 C. Spaas, R. Dok, O. Deschaume, B. De Roo, M. Vervaele, J. W. Seo, C. Bartic, P. Hoet, F. Van den Heuvel, S. Nuyts, W. Seo, C. Bartic, P. Hoet, F. Van Den, R. Dok, O. Deschaume, B. De Roo, M. Vervaele, J. W. Seo, C. Bartic, P. Hoet, F. Van den Heuvel, S. Nuyts, W. Seo, C. Bartic, P. Hoet, F. Van Den, R. Dok, O. Deschaume, B. De Roo, M. Vervaele, J. W. Seo, C. Bartic, P. Hoet, F. Van den Heuvel and S. Nuyts, *Radiat. Res.*, 2016, **185**, 384–392.
38 C. He and J. C. L. Chow, *AIMS Bioeng.*, 2016, **3**, 352–361.
39 B. Koger and C. Kirkby, *Phys. Med. Biol.*, 2017, **62**, 8455–8469.
40 K. Haume, P. de Vera, A. Verkhovtsev, E. Surdutovich, N. J. Mason and A. V. Solov'yov, *Eur. Phys. J. D*, 2018, **72**, 116.
41 A. V. Belousov, V. N. Morozov, G. A. Krusanov, M. A. Kolyvanova and A. A. Shtil, *Biophys.*, 2019, **64**, 23–30.
42 D. Peukert, I. Kempson, M. Douglass and E. Bezak, *Med. Phys.*, 2020, **47**, 651–661.
43 E. Loscertales, R. López-Méndez, J. Mateo, L. M. Fraile, J. M. Udias, A. Espinosa and S. España, *Nanoscale Adv.*, 2025, **7**, 1204–1214.
44 H. Nikjoo, S. Uehara, D. Emfietzoglou and F. A. Cucinotta, *Radiat. Meas.*, 2006, **41**, 1052–1074.
45 J. C. L. Chow, *AIMS Biophys.*, 2018, **5**, 231–244.
46 F. Moradi, K. Rezaee Ebrahim Saraee, S. F. Abdul Sani and D. A. Bradley, *Radiat. Phys. Chem.*, 2021, **180**, 109294.
47 J. C. L. Chow, *Nanomaterials*, 2025, **15**, 117.
48 J. C. L. Chow and C. A. Santiago, *Appl. Sci.*, 2023, **13**, 8249.
49 H. N. Tran, J. Archer, G. Baldacchino, J. M. C. Brown, F. Chappuis, G. A. P. Cirrone, L. Desorgher, N. Dominguez, S. Fattori, S. Guatelli, V. Ivantchenko, J. R. Méndez, P. Nieminen, Y. Perrot, D. Sakata, G. Santin, W. G. Shin, C. Villagrasa, S. Zein and S. Incerti, *Med. Phys.*, 2024, 1–17.
50 S. Incerti, I. Kyriakou, M. A. Bernal, M. C. Bordage, Z. Francis, S. Guatelli, V. Ivanchenko, M. Karamitros, N. Lampe, S. B. Lee, S. Meylan, C. H. Min, W. G. Shin, P. Nieminen, D. Sakata, N. Tang, C. Villagrasa, H. N. Tran and J. M. C. Brown, *Med. Phys.*, 2018, **45**, e722–e739.
51 S. Incerti, A. Ivanchenko, M. Karamitros, A. Mantero, P. Moretto, H. N. Tran, B. Mascialino, C. Champion, V. N. Ivanchenko, M. A. Bernal, Z. Francis, C. Villagrasa, G. Baldacchino, P. Gùye, R. Capra, P. Nieminen and C. Zacharatou, *Med. Phys.*, 2010, **37**, 4692–4708.
52 J. Ramos-Méndez, J. Perl, J. Schuemann, A. Mcnamara, H. Paganetti and B. Faddegon, *Phys. Med. Biol.*, 2018, **63**, 105014.
53 S. Incerti, G. Baldacchino, M. Bernal, R. Capra, C. Champion, Z. Francis, S. Guatelli, P. Guèye, A. Mantero, B. Mascialino, P. Moretto, P. Nieminen, A. Rosenfeld, C. Villagrasa and C. Zacharatou, *Int. J. Model. Simul. Sci. Comput.*, 2010, **1**, 157.
54 M. A. Bernal, M. C. Bordage, J. M. C. Brown, M. Davídková, E. Delage, Z. El Bitar, S. A. Enger, Z. Francis, S. Guatelli, V. N. Ivanchenko, M. Karamitros, I. Kyriakou, L. Maigne, S. Meylan, K. Murakami, S. Okada, H. Payno, Y. Perrot, I. Petrovic, Q. T. Pham, A. Ristic-Fira, T. Sasaki, V. Štěpán, H. N. Tran, C. Villagrasa and S. Incerti, *Phys. Medica*, 2015, **31**, 861–874.
55 P. Zygmanski, B. Liu, P. Tsiamas, F. Cifter, M. Petersheim, J. Hesser and E. Sajo, *Phys. Med. Biol.*, 2013, **58**, 7961–7977.
56 H. Rabus, E. Gargioni, W. B. Li, H. Nettelbeck and C. Villagrasa, *Phys. Med. Biol.*, 2019, **65**, 155016.
57 F. Moradi, M. Jalili, K. Rezaee Ebrahim Saraee, M. U. Khandaker and D. A. Bradley, *Radiat. Phys. Chem.*, 2022, **200**, 110278.
58 J. Perl, J. Shin, J. Schümann, B. Faddegon and H. Paganetti, *Med. Phys.*, 2012, **39**, 6818–6837.
59 J. Schuemann, A. L. McNamara, J. Ramos-Méndez, J. Perl, K. D. Held, H. Paganetti, S. Incerti and B. Faddegon, *Radiat. Res.*, 2019, **191**, 125–138.
60 J. Ramos-Méndez, J. A. Laverne, N. Domínguez-Kondo, J. Milligan, V. Štěpán, K. Stefanová, Y. Perrot, C. Villagrasa, W. G. Shin, S. Incerti, A. McNamara, H. Paganetti, J. Perl, J. Schuemann and B. Faddegon, *Phys. Med. Biol.*, 2021, **66**, 175026.
61 J. Ramos-Méndez, N. D. Kondo and T. A. M. Masilela, *TOPAS-nBio v3.0 (OpenTOPAS v4.0)*, 2024.
62 J. Ramos-Méndez, N. Domínguez-Kondo, J. Schuemann, A. McNamara, E. Moreno-Barbosa, B. Faddegon, S. Francisco, M. G. Hospital, H. Medical, J. Ramos-Méndez, N. Domínguez-Kondo, J. Schuemann, A. McNamara, E. Moreno-Barbosa and B. Faddegon, *Radiat. Res.*, 2020, **194**, 351–362.
63 L. Derksen, V. Flatten, R. Engenhart-Cabillic, K. Zink and K. S. Baumann, *Phys. Med. Biol.*, 2023, **68**, 135017.
64 J. Ramos-méndez, W. G. Shin, M. Karamitros, J. Domínguez-, N. H. Tran, S. Incerti, C. Villagrasa, Y. Perrot, S. Okada, E. Moreno-barbosa, B. Faddegon, J. Domínguez-Kondo, N. H. Tran, S. Incerti, C. Villagrasa, Y. Perrot, V. Štěpán, S. Okada, E. Moreno-barbosa, B. Faddegon, J. Domínguez-, N. H. Tran, S. Incerti, C. Villagrasa, Y. Perrot, S. Okada, E. Moreno-barbosa and B. Faddegon, *Med. Phys.*, 2021, **47**, 5919–5930.
65 J. Bian, J. Duran, W. G. Shin, J. Ramos-Méndez, J. C. Sankey, L. Childress, J. Seuntjens and S. A. Enger, *Phys. Med. Biol.*, 2023, **68**, 124002.

66 A. P. Klapproth, J. Schuemann, S. Stangl, T. Xie, W. B. L. And and G. Multhof, *Cancer Nanotechnol.*, 2021, **12**, 1–18.
67 Y. Lin, S. J. McMahon, M. Scarpelli, H. Paganetti and J. Schuemann, *Phys. Med. Biol.*, 2014, **59**, 7675–7689.
68 A. Pashazadeh, A. Boese and M. Friebe, *J. Dermatol. Treat.*, 2019, **30**, 831–839.
69 G. Poludniowski, A. Omar, R. Bujila and P. Andreo, *Med. Phys.*, 2021, **48**, 3630–3637.
70 W. B. Li, A. Belchior, M. Beuve, Y. Z. Chen, S. Di Maria, W. Friedland, B. Gervais, B. Heide, N. Hocine, A. Ipatov, A. P. Klapproth, C. Y. Li, J. L. Li, G. Multhoff, F. Poignant, R. Qiu, H. Rabus, B. Rudek, J. Schuemann, S. Stangl, E. Testa, C. Villagrasa, W. Z. Xie and Y. B. Zhang, *Phys. Medica*, 2020, **69**, 147–163.
71 W. B. Li, M. Beuve, S. Di Maria, W. Friedland, B. Heide, A. P. Klapproth, C. Y. Li, F. Poignant, H. Rabus, B. Rudek, J. Schuemann and C. Villagrasa, *Phys. Medica*, 2020, **80**, 383–388.
72 H. Rabus, M. Zankl, J. M. Gómez-Ros, C. Villagrasa, J. Eakins, C. Huet, H. Brkić and R. Tanner, *Radiat. Meas.*, 2022, **156**, 106822.
73 H. Rabus, W. B. Li, H. Nettelbeck, J. Schuemann, C. Villagrasa, M. Beuve, S. Di Maria, B. Heide, A. P. Klapproth, F. Poignant, R. Qiu and B. Rudek, *Radiat. Meas.*, 2021, **147**, 106637.
74 W. B. Li, H. Rabus, C. Villagrasa and J. Schuemann, *arXiv*, 2024, preprint, arXiv:2403.13813, DOI: 10.12768/zw0r-6z73.
75 J. Zhang, L. Mou and X. Jiang, *Chem. Sci.*, 2020, **11**, 923–936.
76 L. Meng, J. Zhang, H. Li, W. Zhao and T. Zhao, *J. Nanomater.*, 2019, **1**, 4925702.
77 S. M. Mousavi, S. A. Hashemi, S. Mazraedoost, K. Yousefi, A. Gholami, G. Behbudi, S. Ramakrishna, N. Omidifar, A. Alizadeh and W. H. Chiang, *Nanomaterials*, 2021, **11**, 1–27.
78 V. Pellas, D. Hu, Y. Mazouzi, Y. Mimoun, J. Blanchard, C. Guibert, M. Salmain and S. Boujday, *Biosensors*, 2020, **10**, 146.
79 L. Thomas, M. Schwarze and H. Rabus, *Phys. Med. Biol.*, 2024, **69**, 185014.
80 J. Schuemann, A. McNamara, J. Ramos-Méndez, N. Dominguez-Kondo, J. Perl, D. Yoo, N. Henthorn, J. Warmenhoven, S. Ingram and M. J. Merchant, *Med. Phys.*, 2021, **48**, 6.
81 D. Peukert, S. Incerti, I. Kempson, M. Douglass, M. Karamitros, G. Baldacchino and E. Bezak, *Med. Phys.*, 2019, **46**, 983–998.
82 H. N. Tran, J. Ramos-Méndez, W. G. Shin, Y. Perrot, B. Faddegon, S. Okada, M. Karamitros, M. Davídková, V. Štěpán, S. Incerti and C. Villagrasa, *Med. Phys.*, 2021, **48**, 890–901.
83 B. Rudek, A. McNamara, J. Ramos-Méndez, H. Byrne, Z. Kuncic and J. Schuemann, *Phys. Med. Biol.*, 2019, **64**, 175005.
84 M. Pietrzak, H. Nettelbeck, Y. Perrot, C. Villagrasa, A. Bancer, M. Bug and S. Incerti, *Phys. Medica*, 2022, **102**, 103–109.
85 D. Sakata, S. Incerti, M. C. Bordage, N. Lampe, S. Okada, D. Emfietzoglou, I. Kyriakou, K. Murakami, T. Sasaki, H. Tran, S. Guatelli and V. N. Ivantchenko, *J. Appl. Phys.*, 2016, **120**(24), 244901.
86 D. Sakata, I. Kyriakou, S. Okada, H. N. Tran, N. Lampe, S. Guatelli, M. C. Bordage, V. Ivanchenko, K. Murakami, T. Sasaki, D. Emfietzoglou and S. Incerti, *Med. Phys.*, 2018, **45**, 2230–2242.
87 D. Sakata, I. Kyriakou, H. N. Tran, M. C. Bordage, A. Rosenfeld, V. Ivanchenko, S. Incerti, D. Emfietzoglou and S. Guatelli, *Phys. Medica*, 2019, **63**, 98–104.
88 J. Allison, K. Amako, J. Apostolakis, P. Arce, M. Asai, T. Aso, E. Bagli, A. Bagulya, S. Banerjee and G. Barrand, *Nucl. Instrum. Methods Phys. Res., Sect. A*, 2016, **835**, 186–225.
89 P. Lazarakis, S. Incerti, V. N. Ivanchenko, I. Kyriakou, D. Emfietzoglou, S. Corde, A. B. Rosenfeld, M. Lerch, M. Tehei and S. Guatelli, *Biomed. Phys. Eng. Express*, 2018, **4**, 24001.
90 I. Kyriakou, D. Emfietzoglou, V. Ivanchenko, M. C. Bordage, S. Guatelli, P. Lazarakis, H. N. Tran and S. Incerti, *J. Appl. Phys.*, 2017, **122**(2), 024303.
91 I. Kyriakou, V. Ivanchenko, D. Sakata, M. C. C. Bordage, S. Guatelli, S. Incerti, D. Emfietzoglou, I. Kyriakoua, V. Ivanchenko, D. Sakata, M. C. C. Bordage, S. Guatelli, S. Incerti and D. Emfietzoglou, *Phys. Medica*, 2019, **58**, 149–154.
92 F. M. Khan and J. P. Gibbons, *Khan's the Physics of Radiation Therapy*, Lippincott Williams & Wilkins, 5th edn, 2014.
93 S. N. M. Nawi, M. U. Khandaker, D. A. A. Bradley, S. F. F. A. F. A. Sani, K. S. S. Almugren and A. Sulieman, *Food Bioprod. Process.*, 2020, **106**, 107860.
94 M. C. Fuss, D. Boscolo, M. Durante, E. Scifoni and M. Kramer, *Phys. Med. Biol.*, 2020, **65**, 075008.
95 K. V. Morozov, M. A. Kolyvanova, M. E. Kartseva, E. M. Shishmakova, O. V. Dement'eva, A. K. Isagulieva, M. H. Salpagarov, A. V. Belousov, V. M. Rudoy, A. A. Shtil, A. S. Samoylov and V. N. Morozov, *Nanomaterials*, 2020, **10**, 1–16.
96 S. T. Perkins, D. E. Cullen, M. H. Chen, J. Rathkopf, J. Scofield and J. H. Hubbell, *Tables and Graphs of Atomic Subshell and Relaxation Data Derived from the LLNL Evaluated Atomic Data Library (EADL), Z= 1–100*, Lawrence Livermore National Lab., CA (United States), 1991, vol. 30.
97 H. Rabus, P. Hepperle, C. Schlueter, A. Hloskovsky and W. Y. Baek, *Phys. Scr.*, 2023, **98**, 055015.
98 W. G. Shin, J. Ramos-Mendez, N. H. Tran, S. Okada, Y. Perrot, C. Villagrasa and S. Incerti, *Phys. Medica*, 2021, **88**, 86–90.
99 F. Chappuis, V. Grilj, H. N. Tran, S. A. Zein, F. Bochud, C. Bailat, S. Incerti and L. Desorgher, *Phys. Medica*, 2023, **108**, 1–8.
100 H. N. Tran, F. Chappuis, S. Incerti, F. Bochud and L. Desorgher, *Int. J. Mol. Sci.*, 2021, **22**, 6023.
101 J. Schuemann, R. Berbeco, D. B. Chithrani, S. H. Cho, R. Kumar, S. J. McMahon, S. Sridhar and S. Krishnan, *Int. J. Radiat. Oncol., Biol., Phys.*, 2016, **94**, 189–205.
102 L. Derksen, S. Adeberg, K. Zink and K. S. Baumann, *Phys. Med. Biol.*, 2024, **69**, 03NT01.
103 E. Mansouri, S. Rajabpour and A. Mesbahi, *BMC Chem.*, 2024, **18**, 206.

104 P. Clifford, N. J. B. Green, M. J. Oldfield, M. J. Pilling and S. M. Pimblott, *J. Chem. Soc., Faraday Trans. 1*, 1986, **82**, 2673–2689.
105 M. J. Berger, J. S. Coursey, M. A. Zucker and J. Chang, *NIST Physics Laboratory*, Gaithersburg, MD, 1998, **https://physics.nist.gov/Star**.
106 D. Adjei, N. D. Trinh and M. Mostafavi, *J. Radiat. Res.*, 2023, **64**, 369–378.
107 S. Le Caër, *Water*, 2011, **3**, 235–253.
108 J. Antunes, H. Rabus, F. Mendes, A. Paulo and J. M. Sampaio, *Radiat. Phys. Chem.*, 2025, **232**, 112637.
109 P. Zygmanski, E. Sajo and D. Brivio, *Z. Med. Phys.*, 2023, **33**, 119–122.